

Article

Flood Mapping in a Complex Environment Using Bistatic TanDEM-X/TerraSAR-X InSAR Coherence

Chayma Chaabani ^{1,*}, Marco Chini ², Riadh Abdelfattah ^{1,3}, Renaud Hostache ² 
and Karem Chokmani ⁴ 

¹ Higher School of Communications of Tunis COSIM Lab, University of Carthage, 2083 Tunis, Tunisia; riadh.abdelfattah@supcom.tn

² Environmental Research and Innovation Department (ERIN), Luxembourg Institute of Science and Technology (LIST), L-4422, Belvaux, Luxembourg; marco.chini@list.lu (M.C.); renaud.hostache@list.lu (R.H.)

³ Department of ITI, IMT-Atlantique Bretagne-Pays de la Loire, 29238 Brest cedex 03, France

⁴ Institut National de la Recherche Scientifique, Centre Eau Terre Environnement, 490 rue de la Couronne, Québec, QC G1K 9A9, Canada; karem.chokmani@ete.inrs.ca

* Correspondence: chayma.chaabani@supcom.tn; Tel.: +216-28-489-627

Received: 12 September 2018; Accepted: 6 November 2018; Published: 23 November 2018



Abstract: In this paper, we assess the flood mapping capabilities of the X-band Synthetic Aperture Radar (SAR) imagery acquired by the bistatic pair TanDEM-X/TerraSAR-X (TDX/TSX). The main objective is to investigate the added value of the bistatic TDX/TSX Interferometric Synthetic Aperture Radar (InSAR) coherence in addition to the SAR backscatter in the context of inundation mapping. As a classifier, we consider a Random Forest (RF) classification scheme using TDX/TSX SAR intensities and their bistatic InSAR coherence to extract the flood extent map. To evaluate the classification results and as no “ground truth” was available at the SAR data acquisition time, we set up a LISFLOOD-FP hydraulic model for simulating the temporal evolution of the flood water. The flood map simulated by the model shows good performances with an Overall Accuracy (OA) of 97.92% and a Critical Success Index (CSI) of 94.01%. The SAR-derived flood map is then compared to the LISFLOOD-FP extent map simulated at the SAR data acquisition time. As a test case, we consider the flooding event of the Richelieu River that occurred in the Montérégie region of Quebec (Canada) from April to June 2011. Experimental results highlight the potential of the bistatic InSAR coherence for more accurate flood mapping in a complex landscape with urban and vegetation areas. The classification results of the SAR-derived flood map with respect to the LISFLOOD-FP flood map reach an OA of 78.65% and a Precision of 82.08% when integrating the bistatic InSAR coherence. These classification OA and Precision values are 69.63% and 64.52%, respectively, using only the TDX/TSX SAR intensity.

Keywords: TanDEM-X; TerraSAR-X; bistatic SAR; bistatic InSAR coherence; Random Forest; flood mapping; hydraulic modelling; Richelieu River

1. Introduction

Over the past decade, inundations have accounted for 56% of all climate-related disasters that have had severe environmental and social impacts worldwide [1]. During the period 1970–2014, the estimated flood costs in Canada represented about 78% of the total amount provided by the Disaster Financial Assistance Arrangements (DFAA) [2]. From April to June 2011, a historic flood hit the Montérégie region of Quebec (Canada) and water reached record levels in the Richelieu River. The heavy spring snowmelt and the intense rainfall were the main causes of this unprecedented inundation. This unexpected natural disaster affected approximately 3927 people and 11 municipalities, and Montérégie declared a local state of emergency [3]. This shows that appropriate management

approaches are necessary to minimize the social and economic losses due to floods. A relevant step in this process is to have access to reliable and precise information on the flood extent to execute the rescue activities effectively.

In recent years, many studies have shown the potential of microwave remote sensing in the context of flood detection [4]. In particular, spaceborne Synthetic Aperture Radar (SAR) systems are suitable tools for flood mapping thanks to their daytime and nighttime and almost all-weather imaging capability, in addition to their sensitivity to surface roughness and to soil moisture changes [5]. In the field of remote sensing imagery, many image processing approaches have been implemented using SAR data to delineate the flooded areas [6–8]. In this context, in the case of bare soil, the main premise is the existence of specular reflection from the smooth water bodies which produces a low radar backscattering signal [9]. Among different approaches, the backscattering thresholding is undoubtedly the fastest and most frequently applied technique. Generally, the threshold is identified as a maximum backscatter value that can be associated with open water, in the case where only the flood image is used. However, if an appropriate reference image is available [10], the threshold value is represented by the minimum decrease of backscattering that can be attributed to the change class (e.g., inundated pixels) [11]. For instance, Lu et al. [12] applied thresholding on a difference image, derived by change detection between SAR images acquired over the same area at different times before and after the flooding. In these methods, the selection of a unique threshold is not a straightforward task as SAR data are affected by the speckle noise [13–15]. In Bazi et al. [16] a modified Kittler–Illingworth (KI) [17] threshold selection criterion was proposed to differentiate between flooded and non-flooded regions. However, it should be noted that the presence of certain landscape features such as urban or vegetated areas makes flood mapping complex when considering the SAR imagery [18]. The double-bounce scattering, which is related to the multiple reflections from the dihedral reflectors (for example between the horizontal surface and the vertical structures) is a common scattering mechanism in vegetated or urban areas. The presence of flood water beneath the vegetation causes a remarkable increase in the double-bounce effect which allows the detection of flooded vegetation areas. However, this strongly depends on the canopy density, the incidence angle, the frequency, and polarization of the RADAR system [19,20]. The double bounce can also indicate the presence of flood water in urban areas. The detection of flooding in urban areas has been prompted by the launch of high-resolution spaceborne SAR systems, such as TerraSAR-X (TSX) and COSMO-SkyMed (CSK), which allowed a better identification of the double-bounce feature. Mason et al. [21] investigated the possibility of flood detection in urban areas relying on the increase of the backscattering in the double-bounce features and making use of TSX data and a LiDAR Digital Elevation Model (DEM). The detection of this increase relies on the geometrical accommodation between the building facades and the line of sight of the SAR sensor. The backscattering increase is high when the facade is perpendicular to the SAR line of sight and decreases rapidly when moving away from this geometrical configuration. To overcome this issue, Chini et al. [22] and Pulvirenti et al. [23] emphasized the potential of co-event interferometric SAR coherence to detect the presence of floodwater in urban areas. The InSAR coherence represents the degree of correlation between two Single Look Complex (SLC) images from the same orbit and acquired in two different instants with the same acquisition geometry. Usually, urban areas are very stable targets, characterized by high InSAR coherence values, even for large temporal baselines. The presence of floodwater often results in a decrease in coherence, if one of the two images is acquired during the flood event [24–26]. It is highlighted in Chini et al. [22], that high backscattering values together with low co-event InSAR coherence allow the detection of flooded urban areas. Recent studies focus mainly on forest and vegetation mapping using bistatic InSAR coherence information of the TanDEM-X/TerraSAR-X pair [27–29]. However, to our knowledge there is no example in the recent literature that evaluates bistatic TDX/TSX InSAR coherence (Bist. TDX/TSX InSAR Coh.) information for the purpose of flood mapping.

In this paper, we assess the flood mapping capabilities of the X-band Synthetic Aperture Radar (SAR) imagery acquired by the bistatic pair TDX/TSX. The main objective is to investigate the

added value of the Bist. TDX/TSX InSAR Coh. in addition to the SAR backscatter in the context of inundation mapping in a complex environment. We focus on the flood event that occurred in Saint-Jean-sur-Richelieu city of Canada in 2011, which affected different types of land cover classes, such as bare soil, urban and vegetation areas. We set up a hydraulic model that simulates the temporal evolution of the water level in the Richelieu River during the flood period. The hydraulic model results provide an insight into the flooding extent at the time of the TDX/TSX bistatic image acquisitions. Subsequently, a comparison between the hydraulic model-derived and the SAR/InSAR-derived flood maps is carried out. The paper is organized as follows: in Section 2, the study area and the available dataset are described. In Section 3 the multi-temporal response behavior of SAR intensity and Bist. TDX/TSX InSAR Coh. is discussed for different land covers in the study region. In Section 4, the supervised classification scheme that we use for flood map creation and the validation measures used for the performance assessments are introduced. In Section 5 the Richelieu River model is presented. In Section 6, the results about the comparison of the flood maps derived from the SAR/InSAR images and the hydraulic model simulation are presented. In Section 7, the discussion of results is provided. In the last section, conclusions and perspectives are proposed.

2. Study Area and Dataset

2.1. Study Area

The study area lies in the Southern part of Saint-Jean-sur-Richelieu municipality, which is the regional capital of the Haut-Richelieu MRC, in the Montérégie administrative region of Quebec, Canada (Figure 1). This city occupies an area of 225.6 km² and its population was estimated at 94,846 inhabitants in 2014. Most of the Saint-Jean-sur-Richelieu houses are located on both sides of the Richelieu River [30]. From late April to late June 2011, an unexpected overbanking flow of the Richelieu River occurred, and its magnitude exceeded all other extreme events recorded for at least 100 years in Quebec [31]. This disaster damaged around 2500 main homes in Montérégie. The river exceeded its bankfull discharge due to the combined effect of important snowmelt and extreme spring rainfall that reached approximately 320 mm between early April and late May 2011. The water level increased continuously to reach its peak on 6 May 2011. The maximum flow rate was 1550 m³/s at the “Richelieu aux rapides Fryers” gauging station. On 22 June 2011, the water level of Richelieu River returned to its normal values below bankfull [32].

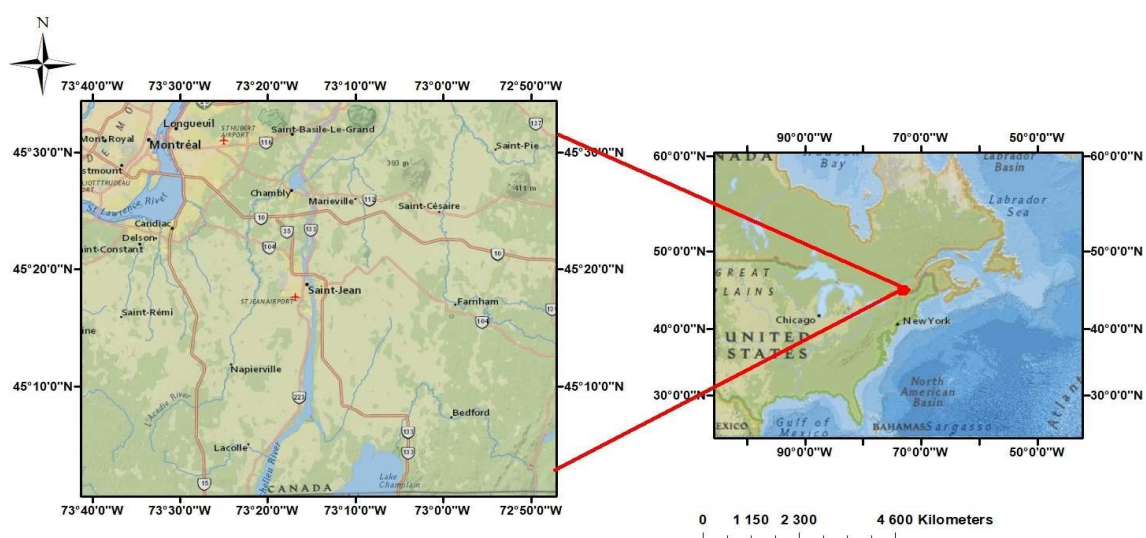


Figure 1. Map of the study area: Saint-Jean-sur-Richelieu, Canada.

2.2. Available Data Set

As no “ground truth” flood extent map was available at the date of the flood bistatic SAR data acquisition, we decided to set up a LISFLOOD-FP hydraulic model in order to cross-evaluate the flood map derived from the bistatic data with the synchronous model result and to reinforce our knowledge of the temporal evolution of the flood extent. The available data used for these purposes are described in Sections 2.2.1 and 2.2.2. The evaluation of the hydraulic model accuracy was performed based on a flood map (Figure 2) that was extracted manually from GeoEye-1 optical image (0.6 m). This image was acquired during the flooding event, on 1 May 2011, 14 days prior to the SAR images acquisition.

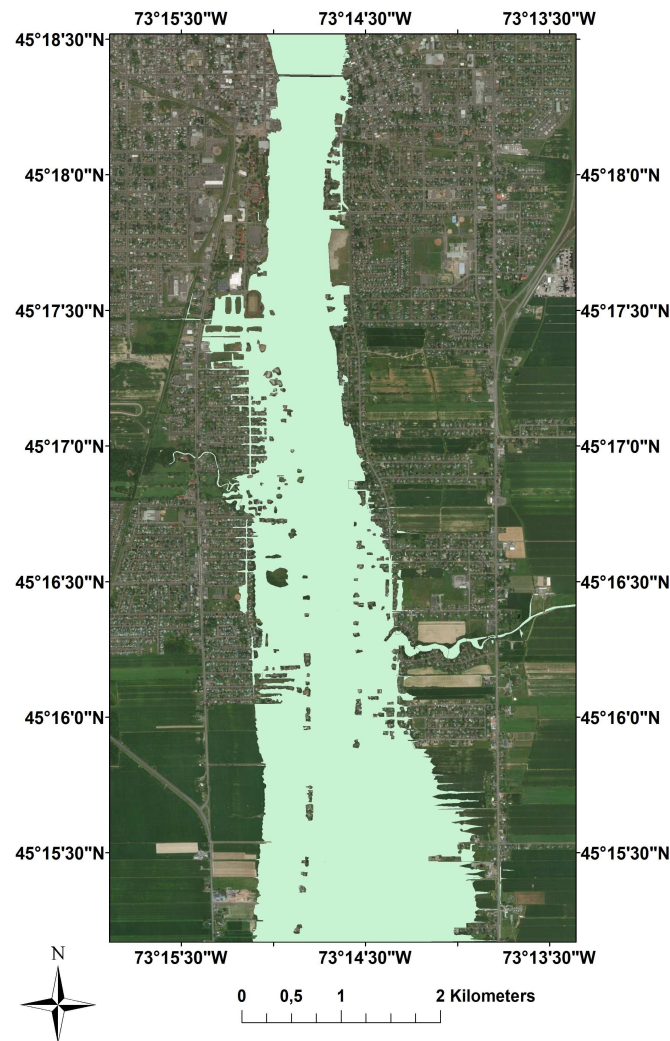


Figure 2. Flood map extracted manually from the GeoEye-1 optical image (0.6 m).

2.2.1. Synthetic Aperture RADAR Data

The high-resolution SAR images used for this study were obtained thanks to a science proposal submission for data request from the TanDEM-X Science Service System (Proposal ID HYDR7130). The German spaceborne TanDEM-X (TerraSAR-X add-on for Digital Elevation Measurements) was launched in 2010 and its mission concept is to provide cooperative performance capabilities to the TerraSAR-X mission. Both satellites perform simultaneous imaging of the earth through the X-band wavelength (3 cm). The main goal of the TanDEM-X mission is to generate a worldwide high precision DEM. In addition, several experiments of across and along-track SAR interferometry

applications are included in the bistatic TanDEM-X/TerraSAR-X mission namely, land cover, hydrology, and oceanography [33].

A set of three multi-temporal stripmap (3m resolution) bistatic TDX/TSX pairs are used for this study (details in Table 1), the first was acquired during the flood event, the second was acquired after two months and the last one was acquired after more than one year after the event. The available SAR intensities and bistatic TDX/TSX InSAR coherence images are shown in Figure 3. All the three pairs of intensities and their corresponding Bist. TDX/TSX InSAR Coh. were geocoded in a common cartographic system to build the multi-temporal input vector for the per-pixel classification.

Table 1. Bistatic TanDEM-X/TerraSAR-X Interferometric pairs.

Acquisition Time	Acquisition Mode	Polarization	$B_{\text{perpendicular}}$ (m)	Looking Angle
14/05/2011 (during the flood)	Stripmap (Ascending)	HH	318.02	41–43
14/07/2011 (after the flood)	Stripmap (Ascending)	HH	281.36	39–41
29/08/2012 (after the flood)	Stripmap (Ascending)	HH	407.49	40–42

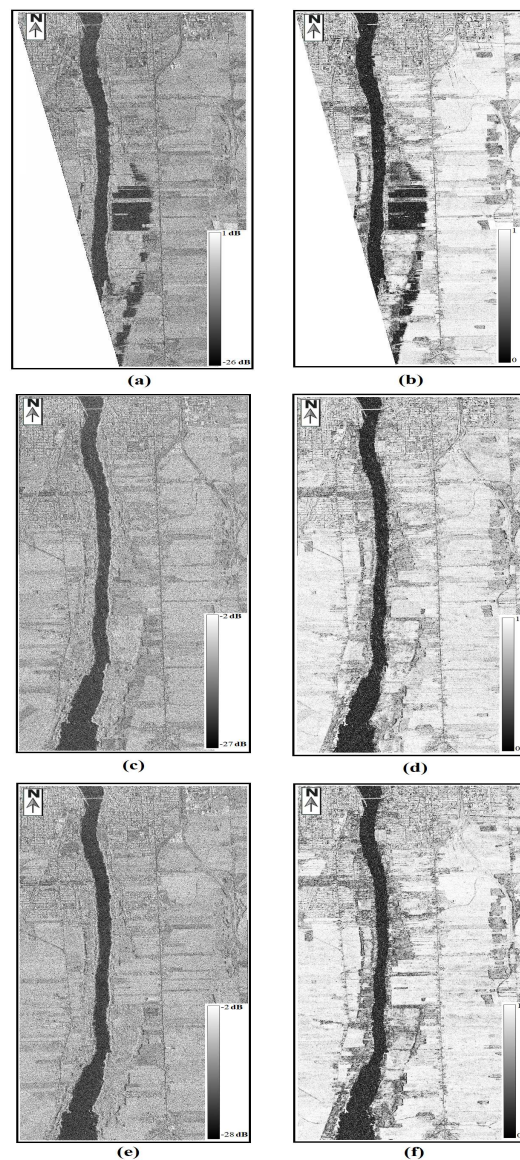


Figure 3. Left column: Intensity SAR Images, right column: bistatic TanDEM-X/TerraSAR-X InSAR coherence data (Color bars represent pixel values): (a,b) May 2011 (during the flood), (c,d) July 2011 (after the flood) and (e,f) August 2012 (after the flood).

2.2.2. Topographic and Hydrometric Data

The hydraulic model set-up requires a set of topographic, bathymetric, and hydrometric data, namely a DEM of the floodplain, the riverstream bathymetry (i.e., riverbed geometry) and the boundary conditions [34]. In this study, the hydrometric information, namely the water level and the streamflow hydrograph, were acquired at the gauging station “Richelieu aux rapides Fryers” for a 6 months period (March to August 2011, see Figure 4). This time frame was chosen so that the model simulation starts at least one month before the beginning of the flood when the flow was still in the riverbed. Figure 5 indicates the position of the gauging station “Richelieu aux rapides Fryers”. Furthermore, a LiDAR DEM representing the topography of the floodplain in the study area and bathymetric data (dense sampling point cloud) was acquired using an echo-sounder.

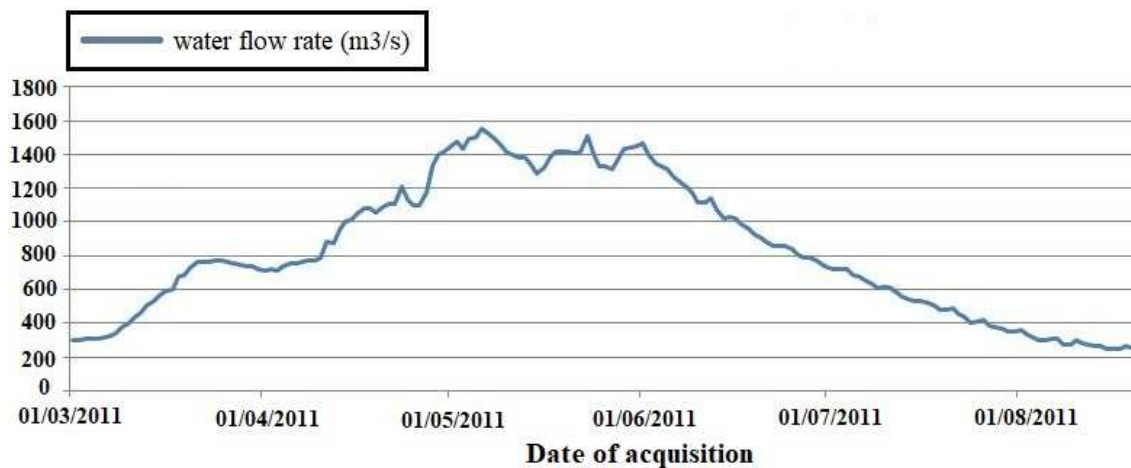


Figure 4. Streamflow hydrograph recorded at gauging station of “Richelieu aux rapides Fryers”.

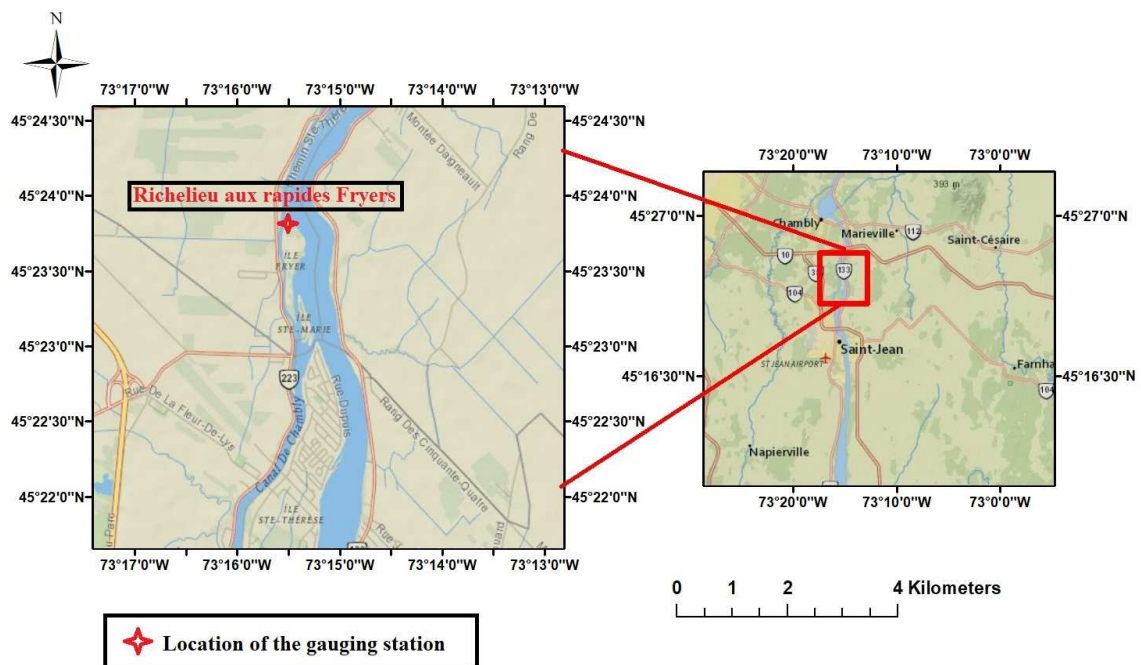


Figure 5. Overall view of the study area and location of the gauging station “Richelieu aux rapides Fryers”.

3. Data Analysis

Based on a visual analysis of the optical satellite images of the study area, it is possible to identify 10 different Regions Of Interest (ROI) as displayed in Figure 6. The selection of ROIs samples from

SAR and Bist. TDX/TSX InSAR Coh. images were done based on the 3D view offered by Google Earth. All these ROIs describe the landcover types that existed in the study region during the flood. We notice that both flooded and non-flooded states can be observed for the same landcover especially for agricultural and vegetated zones. The selected ROIs for this study are defined as follows:

- River: represents different parts of the Richelieu River stream.
- Dry agriculture: represents agricultural zones that remained dry and not affected by the flooding.
- Flooded agriculture: represents the agricultural zones in the river floodplain that were submerged.
- Dry vegetation: represents mainly forest zones that remained dry and not affected by the flooding.
- Flooded vegetation: represents mainly forest zones that were affected by the presence of water during the flood.
- Dry urban zone: represents the urban zone of Saint-Jean-sur-Richelieu city with a dense building topology.
- Dry roads: represents the roads that were not affected by the flooding.
- Dry grass: mainly represents grass (e.g., in public parks or house gardens) that was not affected by flood water.
- Building roofs: represents only the roofs of houses and buildings.
- Flooded residential: represents the residential areas lying in the river floodplain that were identified as flooded during the event. We can notice that the building structure within this ROI is very different when compared to the Dry Urban ROI as the buildings here are mainly sparsely distributed houses.

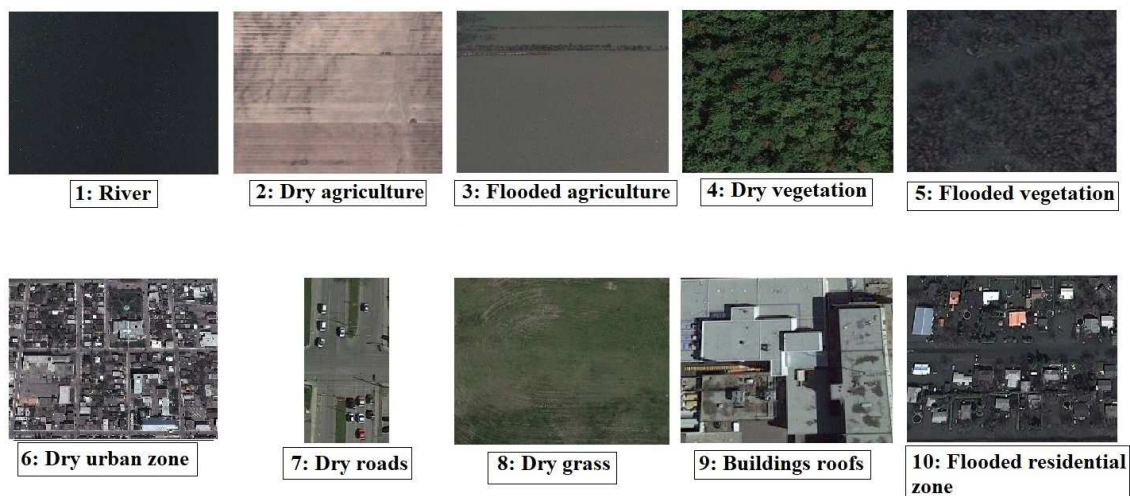


Figure 6. Selected Regions of Interest for the study area.

To show the multi-temporal response of the different land covers according to the presence or absence of water and to highlight the role of the Bist. TDX/TSX InSAR Coh. with respect to the solo SAR intensity, the average values of intensity and Bist. TDX/TSX InSAR Coh. for the different selected ROIs are plotted in Figure 7. Table 2 reports the average and standard deviation values of intensity and Bist. TDX/TSX InSAR Coh. within each selected ROI.

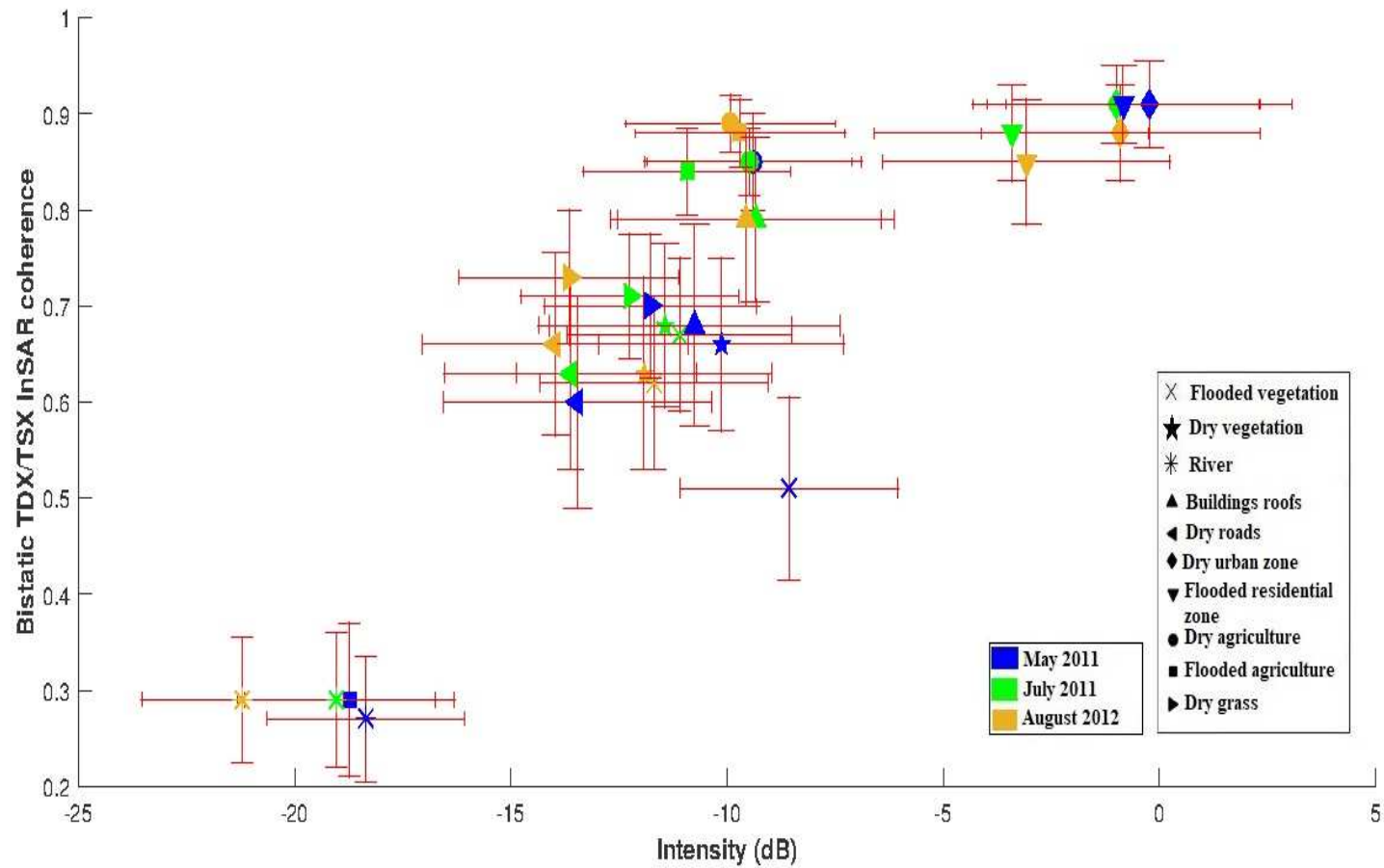


Figure 7. The general scatter plot with standard deviation error bars of multi-temporal SAR intensity and Bistatic InSAR coherence values for TanDEM-X/TerraSAR-X data.

Table 2. Average and standard deviation (between parentheses) values of the intensity and bistatic InSAR coherence within the selected ROIs (Coh. = coherence).

Date	May 2011 (Flooding Period)		July 2011		August 2012	
	Intensity	InSAR Coh.	Intensity	InSAR Coh.	Intensity	InSAR Coh.
1: River	−18.36 (4.56)	0.27 (0.13)	−19.04 (4.59)	0.29 (0.14)	−21.21 (4.65)	0.29 (0.13)
2: Dry agriculture	−9.54 (5.02)	0.85 (0.1)	−9.46 (4.72)	0.85 (0.07)	−9.92 (4.86)	0.89 (0.06)
3: Flooded agriculture	−18.73 (4.85)	0.29 (0.16)	−10.93 (4.79)	0.84 (0.09)	−9.69 (4.84)	0.88 (0.07)
4: Dry vegetation	−10.13 (5.67)	0.66 (0.18)	−11.43 (5.87)	0.68 (0.17)	−11.92 (5.9)	0.63 (0.2)
5: Flooded vegetation	−8.56 (5.04)	0.51 (0.19)	−11.10 (5.19)	0.67 (0.16)	−11.68 (5.27)	0.62 (0.18)
6: Dry urban	−0.24 (6.6)	0.91 (0.09)	−1.05 (6.64)	0.91 (0.08)	−0.9 (6.46)	0.88 (0.1)
7: Dry roads	−13.46 (6.2)	0.6 (0.22)	−13.62 (5.85)	0.63 (0.2)	−13.97 (6.15)	0.66 (0.19)
8: Dry grass	−11.77 (4.92)	0.7 (0.15)	−12.25 (5.04)	0.71 (0.13)	−13.65 (5.09)	0.73 (0.14)
9: Buildings roofs	−18.36 (6.71)	0.27 (0.21)	−19.04 (6.4)	0.29 (0.17)	−21.21 (6.26)	0.29 (0.18)
10: Flooded residential	−0.87 (6.31)	0.91 (0.08)	−3.47 (6.35)	0.88 (0.1)	−3.13 (6.65)	0.85 (0.13)

It is worth noting that the Bist. TDX/TSX InSAR Coh. is affected by the same sources of decorrelation as the multipass InSAR coherence, which are a limited signal-to-noise ratio, a quantization error, a spatial baseline decorrelation, a temporal decorrelation, and a volumetric decorrelation. Although multipass and bistatic InSAR coherences share some similarities with respect to the coherence degradation, the magnitude of this degradation is different from one configuration to another. An example is the temporal decorrelation that is negligible in a bistatic acquisition but is used for detecting changes in multipass acquisition. For bistatic acquisitions, the TDX/TSX along-track baseline is usually smaller than 600m, resulting in a temporal baseline of 40 ms [29,35]. As a result, flooded buildings should have high coherence values, even higher than unflooded ones, as the signal-to-noise ratio increases due to increased backscattering caused by double bounce. An opposite behavior is expected for open water, since it is characterized by low levels of signal-to-noise ratio, due to poor backscatter returns, resulting in a strongly degraded interferometric coherence. The backscatter values of calm waters, due to the specular reflection of the SAR signal, are often close to the system sensitivity [29,35].

Looking at Figure 7, the above considerations are consistent with the values of intensity and coherence for the different land cover classes. Moreover, dry vegetation, which is affected mainly by volumetric decorrelation has coherence values in the range [0.6–0.7], while dry agriculture has a higher value.

As can be expected, the intensity and the coherence values of the flooded agriculture class are significantly lower than those of the dry one, whereas for the vegetation class, the presence of water induces a slight increase of the backscattering and a decrease of the coherence. This can be attributed to the vegetation type, which is not very dense, so that the coherence can be affected by the direct return from the water surface.

Concerning the agricultural zone, it is important to mention that the farms of Saint-Jean-sur-Richelieu are mainly oriented towards cereal production and that the grain seed plantation starts in Mid-May. This means that, at the date of the SAR image acquisition in May 2011, the Flooded agriculture ROI can be seen as a bare soil submerged by water. In Figure 7, a detailed analysis of the agriculture ROIs can be done. In fact, we observe that the Flooded agriculture ROI has backscattering values similar to those of the River ROI, indicating a specular reflection. Furthermore, we can notice a Bist. TDX/TSX InSAR Coh. value decrease of approximately 0.6 at the flooding date. Obviously, the use of bistatic InSAR coherence information in this case reinforces the possibility of distinguishing the flooded agriculture regions. The scatter plot in Figure 7 shows that although the changes in the backscattering values for each landcover class due to the presence of water are as expected, they do not provide sufficient information to easily classify flooded and unflooded regions, especially in more complex landcover classes such as vegetation and urban areas. However, it shows that the Bist. TDX/TSX InSAR Coh. is an important source of information to improve the flood detection. In this context, it is worth highlighting the importance of Bist. TDX/TSX InSAR Coh. as an added feature for flood mapping purposes. Indeed, it is often difficult to find very high-resolution

SAR images of the same orbit to calculate the multi-temporal coherence as a change detection feature. It is even more difficult to find a multipass interferometric pair with a very short temporal baseline, which allows the change detection analysis and avoids the usual temporal decorrelation, especially in the case of a shorter wavelength such as the X-band.

4. Random Forest Classification Approach

Section 3 concludes that the use of TDX/TSX intensity together with Bist. TDX/TSX InSAR Coh. could provide additional insight on the flooded scene and should help in the floodwater classification. To this end, we apply a classification scheme that interprets this information. The overall objective of classification in the context of remote sensing imagery is to categorize all image pixels into land cover themes. In this study, we use a Random Forest (RF) classifier [36], to generate the flood map of Saint Jean Sur-Richelieu. The advantages of the RF classification, over other supervised classification methods, are specified in the literature of remote sensing imagery such as in Myint and Okin [37] and Liu and Yang [38]. The RF approach gained more widespread use for different environmental and agricultural purposes. For instance, Sonobe et al. [39] used the RF classification of multi-temporal TerraSAR-X dual-polarimetric data to identify the crop type. In Dubeau et al. [40], the RF classification was used to monitor the Dabus Wetlands in Ethiopia using a combination of multispectral optical, RADAR and topographic data. In the context of flood mapping, Feng et al. [41] used the RF classifier with medium resolution optical imagery. The use of the Random Forest algorithm for TerraSAR-X data classification has already proved successful by Wohlfart et al. [42], a study that reviewed most articles published in the past decade, incorporating TerraSAR-X information into wetland.

In this study, we use the RF classification to differentiate the landcover types of the flooded region using multi-temporal input data of TDX/TSX SAR intensity and their corresponding Bist. TDX/TSX InSAR Coh. Actually, the RF classifier is robust to the outliers of the training dataset. Unlike statistical approaches, Random Forest does not make assumptions about the training data distributions. This is an advantage considering the input space composed of non-homogeneous data [43,44]. RF is based on a set of decision-tree classifiers in which a majority rule is imposed to enhance the classification performance [45]. The main concept of the Random Forest approach is the use of Bootstrap Aggregating (aka bagging) [46] which is based on averaging the predictions of several non-parametric models (decision-tree classifiers) to reduce the variance without increasing the bias. The predictive model of decision trees [47] has a hierarchal structure that contains a set of nodes which allows the learning of simple decision rules that are inferred from the data features. The decision-tree leaves represent the class labels and the branches are the conjunctions of features that lead to the desired class labels. The two parameters that play an important role in the RF algorithm are the size of the training sample and the number of decision trees. In this study, we propose to carry out a sensitivity analysis of the RF algorithm for these two parameters in Section 6.

Evaluation Measures

The performance assessment of the flood mapping approach is done based on different validation coefficients related to the confusion matrix analysis (Table 3). We mainly use the Overall Accuracy (OA), the Critical Success Index (CSI) and the Precision index (Equation (1)). The OA coefficient gives an overall indication about the model and ground truth matching. The CSI is relevant for evaluating flood maps as it does not take into account the information of “true negative”. As our main interest is the flooded surfaces that were correctly detected, we are not focusing on the efficiency of detecting the non-flooded surfaces. The Precision index gives an idea about the correct prediction rate of the positive values (flood). It shows how often the model is correct when the flooded surfaces are detected.

$$OA = \frac{a + d}{a + b + c + d} \quad CSI = \frac{a}{a + b + c} \quad Precision = \frac{a}{a + b} \quad (1)$$

Table 3. Confusion Matrix.

		Ground Truth	
		Flood	No Flood
Model	Flood	<i>a</i> : True positive	<i>b</i> : False positive
	No Flood	<i>c</i> : False negative	<i>d</i> : True negative

5. Hydraulic Model Set-Up

Besides the use of SAR and Bist. TDX/TSX InSAR Coh. images to delineate the flood extent, we set up a hydraulic model based on the LISFLOOD-FP software [48] for simulating the temporal evolution of the flood waters in the Richelieu River and therefore cross evaluating the SAR-derived flood extent map. LISFLOOD-FP is a 2D raster-based model that simulates the water flow propagation in riverbeds and floodplains using the finite-difference method to solve a reduced form of the shallow water equations [49]. In the study of Afshari et al. [50], it is argued that a 2D model can provide accurate estimation of inundation extents during severe floods. This lends weight to the use of simulated flood extent maps as a reference for evaluating the remote sensing-derived flood maps. Many works investigated the computational efficiency and the validity of LISFLOOD-FP model. For instance, Neal et al. [51] evaluated LISFLOOD-FP in the context of monitoring the summer 2007 floods around the city of Tewkesbury, UK. In Van der Sande et al. [52], the authors integrated remote sensing imagery information to calibrate LISFLOOD-FP model to produce the Manning coefficient of the Meuse river during the 1995 flooding in Netherlands. Furthermore, Wood et al. [53] used medium resolution SAR data to calibrate LISFLOOD-FP hydraulic model and to obtain the River Severn channel depth and friction parameters during several floods in the UK. Hostache et al. [54] assimilated the satellite-derived flood extent maps into LISFLOOD-FP to reduce forecast uncertainties.

As usual for hydraulic models, LISFLOOD-FP requires topographic, bathymetric, and hydrometric data, namely, floodplain DEM, channel bathymetry and boundary conditions. In this study, the upstream streamflow and downstream water level hydrographs are defined as boundary conditions. These two hydrographs are both derived from the “Richelieu aux rapides Fryers” gauging station dataset as the flood wave travel time is very short between the upstream and the downstream boundaries of the model. The main calibration parameter of a 2D hydraulic model is the Manning friction coefficient. In fact, the model sensitivity to this parameter can be relatively limited [55] especially for 2D models. However, in this study, the friction coefficients were not calibrated but rather taken from the study of Oubennaceur et al. [56] where a calibration was carried out over the same area of interest, but with another 2D hydraulic model. The availability of very high-resolution topographic and bathymetric data (see Section 2.2.2) enabled us to set up the flood model of Richelieu River at 6 m spatial resolution. We use this model to simulate daily flood maps during 6 months (March to August 2011). Figure 8 shows the simulated water depth maps at different dates from March 2011 to May 2011. To validate the model results, we compare the simulated flood map with a flood extent map observed on 8 May 2011 that was manually delineated from a GeoEye-1 image (Figure 2). Both the Overall Accuracy (OC) coefficient and the CSI were calculated to validate the model results. The CSI measure is chosen for the flood model evaluation because its calculation does not include the “correct rejections” (“correct no water”) values. This means that it focuses only on the evaluation of the prediction performances of the water areas [53]. Table 4 reports the performance values computed for the LISFLOOD-FP model of the Richelieu River flooding. The high values in Table 4 indicate a really good performance of the set-up model in terms of simulated flood extent and lends more weight to the use of simulated flood extent maps as a reference for evaluating the remote sensing-derived flood maps. Figure 9 shows the Google Earth projection of the flood extent on 14 May 2011 (date of the flood SAR acquisition) derived from the water levels as simulated by the LISFLOOD-FP hydraulic model. This map is used as a reference for the SAR/InSAR-derived flood maps evaluation.

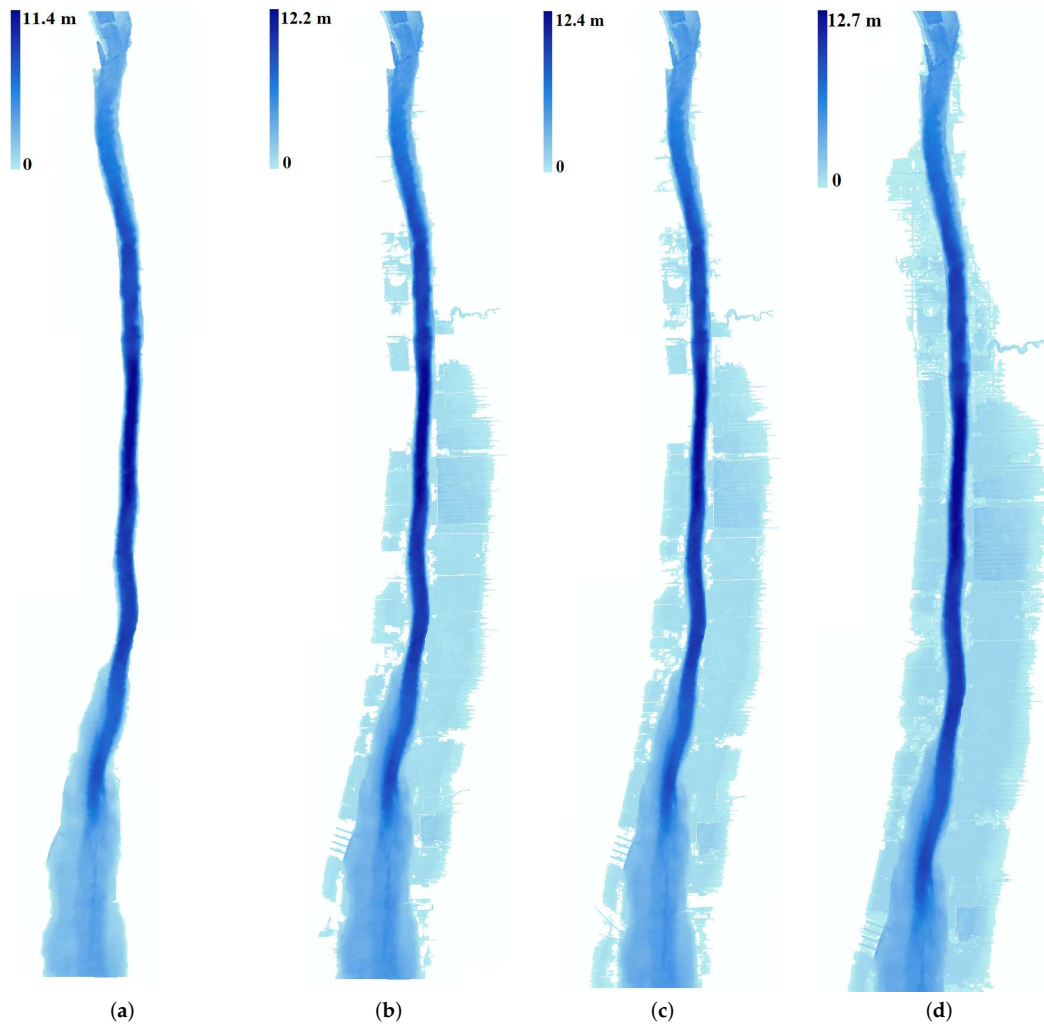


Figure 8. Temporal evolution of water depth as simulated using LISFLOOD-FP model: (a) 13 March 2011 (before the flooding), (b) 15 April 2011 (during the flooding), (c) 22 April 2011 (during the flooding), (d) 14 May 2011 (during the flooding).

Table 4. Performance measures of Richelieu River LISFLOOD-FP model.

	Critical Success Index (CSI)	Overall Accuracy (OA)
performance value	94.01%	97.92%

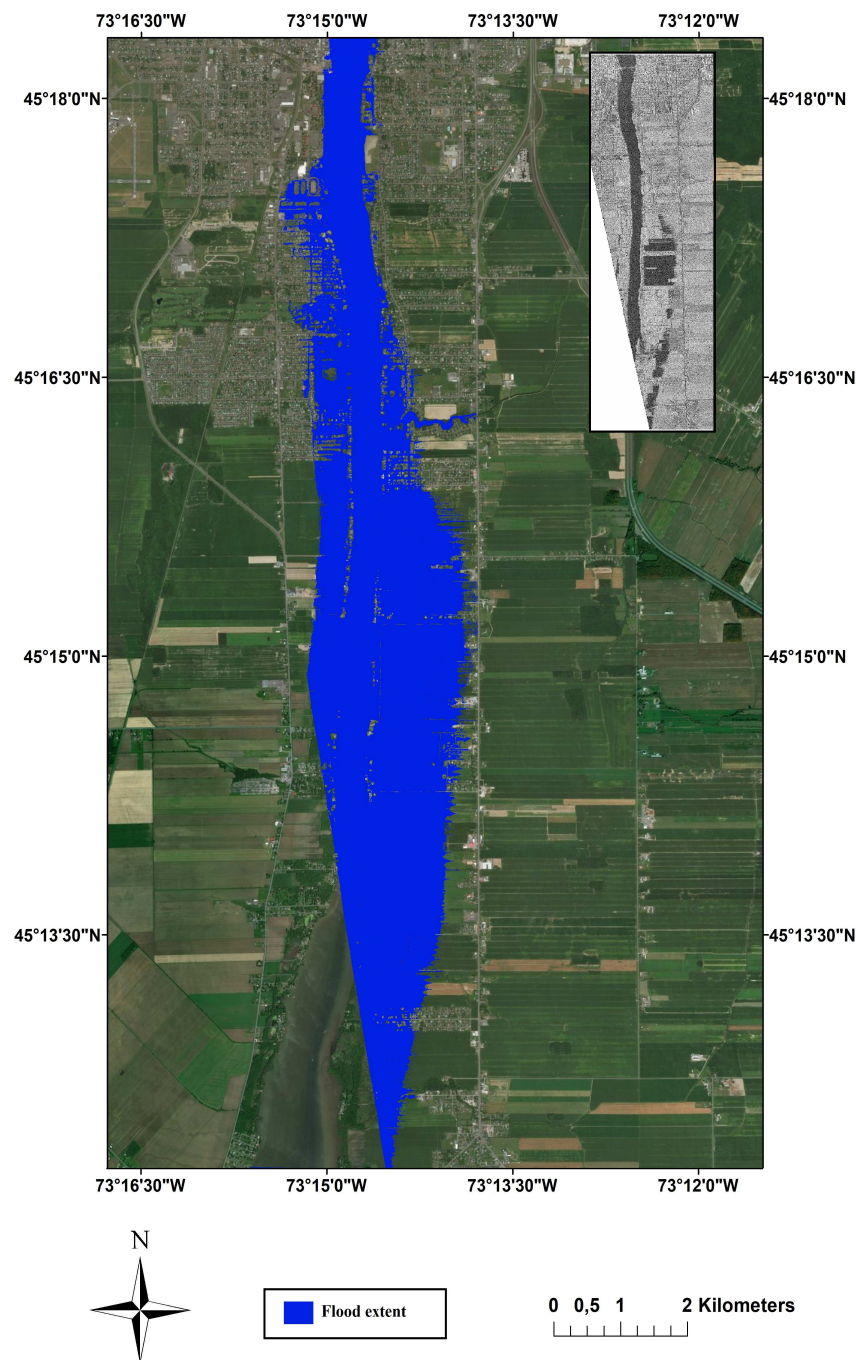


Figure 9. Google Earth projection of the flood extent (derived from the water depth simulated by the LISFLOOD-FP model) on 14 May 2011 that is considered to be “ground truth”: the flood extent that corresponds to the time of SAR data acquisition (at the top right corner).

6. Results

As mentioned in Section 4, the Random Forest classifier uses as input the geocoded set of multi-temporal intensity and Bist. TDX/TSX InSAR Coh. data. To determine the best training parameters, Table 5 presents the RF classification result evaluation based on the simulated flood extent map (see Section 5) using different numbers of training samples and decision trees. For each training set-up, the Overall Accuracy and Precision performance measures were calculated. It is

worth noting that the Precision index was chosen for the classification evaluation in this study since it can specifically show the reliability of the flooded class. In the context of classification accuracy assessment for remotely sensed data, the Precision metric is considered to be the User's accuracy [57] and represents the fraction of properly classified flooded pixels with regard to all pixels that were identified as flooded in the image. The results of the Random Forest classification using the training samples from the 10 selected ROIs are considered as a map that contains a set of flooded classes for different landcover groups. The final purpose of the classification is to distinguish flooded and non-flooded areas. Thus, we carry out the evaluation of the classification based on the flood extent map simulated by the LISFLOOD-FP hydraulic model at the acquisition time of the satellite data during the flood (14 May 2011). It is, therefore, necessary to group the 10 classes of the classification into two different semantic groups: flooded and non-flooded (the flooded class also contains permanent water from the river). To do this, all the pixels that are classified as flooded (River, Flooded agriculture, Flooded residential zone and Flooded vegetation), and non-flooded (Dry agriculture, Dry urban, Dry vegetation, Dry roads, Dry grass and Buildings roofs) ROIs, are merged in two separate classes. All the classification tests presented in Table 5 show a significant improvement of the Overall Accuracy and Precision measures when using the combination of multi-temporal Intensity and Bist. TDX/TSX InSAR Coh. data. Furthermore, we notice that when the numbers of training samples and decision trees increase, the classification accuracy is improved. Besides, the saturation is reached for 20,000 training samples and 300 decision trees (highlighted in bold characters in Table 5), which have been selected as the best training parameters to produce the final SAR/InSAR-derived flood map. The first 10,000 samples were used for the training step and the remaining 10,000 samples were used as test samples. The training process is performed based on the decision-tree concept and training samples are trained using the "feature bagging" method where the algorithm selects a random subset of the features. In the classification stage, the trained classifier is used to classify the pixels with known feature values but unknown class by taking the majority vote.

Table 5. Random Forest classification results with various training parameters (decision trees and samples number). Bist. = bistatic, Coh. = coherence.

Multi-Temporal Input Data	Training Parameters		Overall Accuracy	Precision
	Samples Number	Decision Trees		
Intensity only	15,000	100	69.69%	64.97%
Intensity and Bist. TDX/TSX InSAR Coh.	15,000	100	78.69%	80.34%
Intensity only	20,000	100	69.58%	64.65%
Intensity and Bist. TDX/TSX InSAR Coh.	20,000	100	78.59%	81.06%
Intensity only	20,000	300	69.63%	64.52%
Intensity and Bist. TDX/TSX InSAR Coh.	20,000	300	78.65%	82.08%
Intensity only	20,000	500	70.07%	65.64%
Intensity and Bist. TDX/TSX InSAR Coh.	20,000	500	78.66%	81.95%

After processing the RF classification, two contingency maps (Figure 10) are created by overlaying the LISFLOOD-FP model-derived flood extent, serving as a reference, and the SAR/InSAR-derived flood maps that were generated by the RF classification scheme. Figure 10 represents the contingency maps that show the agreement between hydraulic model-derived flood extent and RF classified maps using, respectively, only the multi-temporal TDX/TSX intensity (Figure 10a) and the multi-temporal TDX/TSX intensity with the Bist. TDX/TSX InSAR Coh. data (Figure 10b).

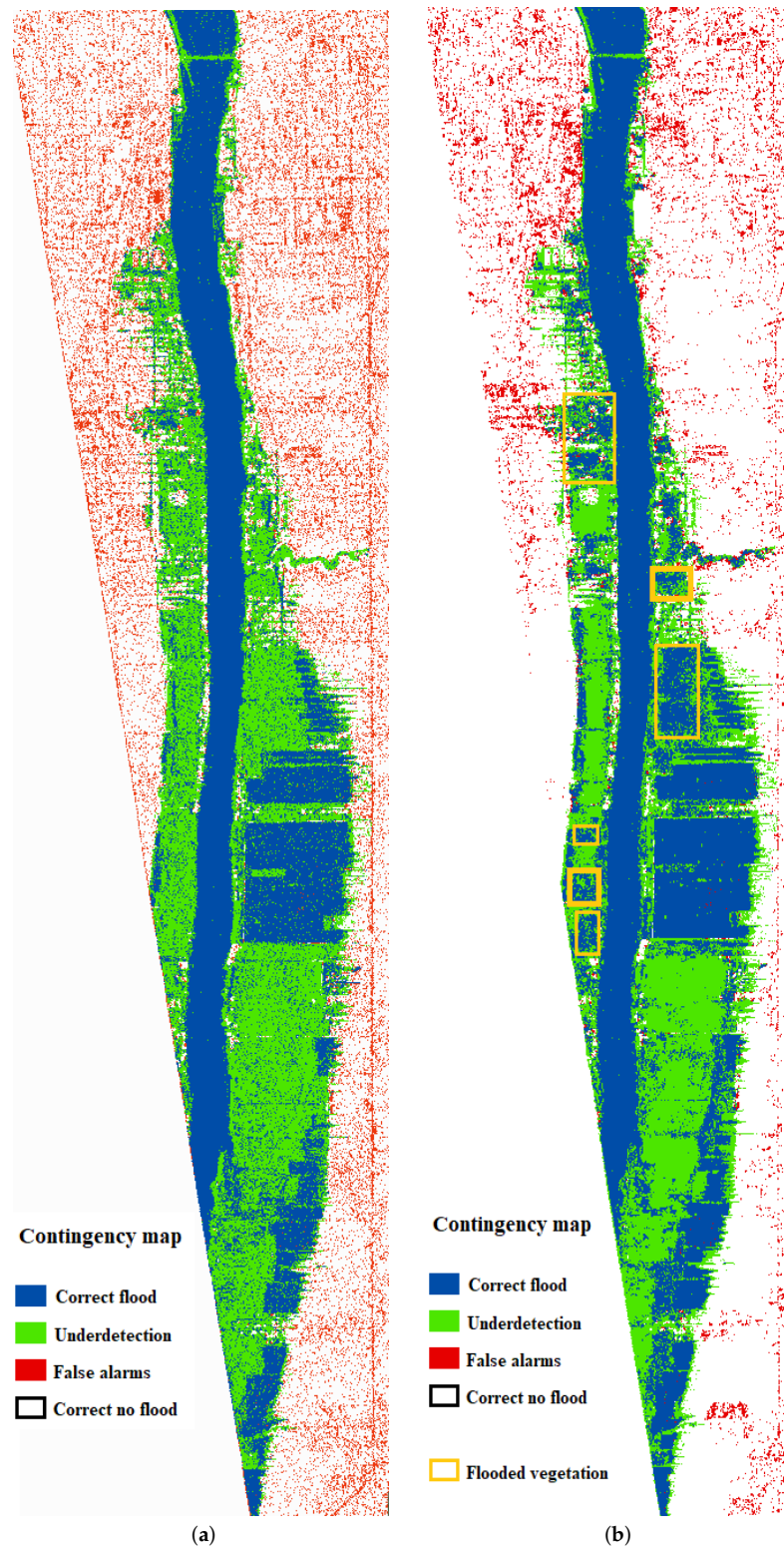


Figure 10. Contingency maps of the LISFLOOD-FP model-derived flood extent and the RF classification results that were created: (a) using only the multi-temporal TDX/TSX intensity (b) using the multi-temporal TDX/TSX intensity and bistatic TDX/TSX InSAR coherence.

7. Discussion

Based on the contingency maps of Figure 10, it can be noticed that the use of Bist. TDX/TSX InSAR Coh. data substantially improves the flood extent map especially when considering the urban,

agriculture and vegetation areas. The yellow rectangles in Figure 10b show some flooded regions of vegetation that were detected by the integration of Bist. TDX/TSX InSAR Coh. data. Although fully polarimetric data are generally recommended to detect flooded vegetation [58,59], the present study identifies the inundated vegetation using the InSAR coherence information of the single polarization (HH) of the bistatic TanDEM-X/TerraSAR-X data. Indeed, the sufficient penetration through the vegetation canopy is among the main factors that increase the double-bounce backscattering effect in case of flooded vegetation. Usually, high wavelength (C-band) and reasonably small incidence angles are preferred to detect the increase of double bounce due to the existence of floodwater beneath vegetation. However, in this study, the presence of relatively sparse canopy of trees and the use of horizontal polarization (HH) guaranteed a deeper penetration to detect the increase of the double-bounce intensity of flooded vegetation.

As a consequence, it can be noticed that the integration of Bist. TDX/TSX InSAR Coh. information allows a significant reduction of under-detection errors, especially in the vegetated areas. When comparing the false alarm rates of Figure 10a,b, we can observe that the over-detection errors are substantially reduced by the integration of Bist. TDX/TSX InSAR Coh. information especially in the dry agriculture regions. However, some of the classification errors remain; as for example the highway “Route 133” (vertical line in Figure 10b) that is erroneously identified as flooded because of the smooth surface of asphalted road which gives low backscatter and can be easily confused with floodwater. Another example is the dense urban settlements in the northern part of the study area where some of the dry pixels are classified as flooded. This highlights that flood mapping in a dense urban environment remains a challenging task because of many factors such as the mutual shadowing and the higher order bounces [19], especially when using the Bist. TDX/TSX InSAR Coh. data that does not provide the change detection information since the temporal baseline between the two acquisitions is a few milliseconds.

Noticeably, the present study gives a relatively straightforward and promising flood mapping approach that takes advantage of the bistatic interferometry of short wavelength (3 cm) X-band data. Among the recent research studies that dealt with inundation mapping for the same flooding event (Richelieu River in 2011) using SAR imagery, the study of Tanguy et al. [32] can be mentioned. The authors used the RADARSAT-2 C-band data with a longer wavelength (5.5 cm) and included information on the flood hazard at each point of the study area to reduce errors in the derived flood extent map. The hazard map is created based on river water heights, topographic elevation data and publicly available return period shorelines in the study area. Tanguy et al. [32] proposed a flood mapping method based on the detection of the maximum extent of the flood by object-based classification of the SAR image. Next a thresholding on the hazard map is applied to remove the non-water pixels erroneously included in the flooded classes. The integration of ancillary information reduces the over-detection rate in urban areas. Figure 8 in Tanguy et al. [32] shows the “open water” objects map derived from the RADARSAT-2 image. In this map, one can observe that the flooded agriculture and vegetation regions are under-detected. This highlights the difficulty to classify flooded areas in urban and vegetated regions. Overall, the study by Tanguy et al. [32] shows that integrating ancillary information related to flood hazard allows the improvement of the identification of these flooded regions (Figure 10 in Tanguy et al. [32]). In the current study, we show that the use of Bist. TDX/TSX InSAR Coh. data allows, in a similar way, a considerable reduction of both under and over-detection in vegetation, agriculture and urban areas. In particular, flooded vegetation (yellow rectangles in Figure 10b) are better classified when integrating the Bist. TDX/TSX InSAR Coh. data.

8. Conclusions

In this study, the flood mapping capacity of bistatic TanDEM-X/TerraSAR-X (X-band) data was investigated in the presence of different landcover types. The main objective was to highlight the valuable information offered by the bistatic TDX/TSX InSAR coherence for accurate flood mapping in areas where solo SAR intensity data has limitations. We used the Random Forest supervised

classification approach on the stack of multi-temporal SAR and InSAR bistatic TanDEM-X/TerraSAR-X data to map flooded and non-flooded areas. As no “ground truth” was available at the SAR data acquisition time, we set up a LISFLOOD-FP hydraulic model at a 6 m resolution for Richelieu River and simulated daily flood extent maps between April 2011 and June 2011. Then, we used the simulated flood extent map as a reference for evaluating the flood maps derived from the SAR/InSAR images. For reliability reasons, the hydraulic model was previously evaluated using a reference flood map derived from an optical satellite image that was acquired a few days before the SAR image acquisition. This evaluation showed the high accuracy of the hydraulic model results ($CSI = 94.01\%$). Furthermore, the important role of the X-band bistatic InSAR coherence for flood mapping was assessed. The classification Overall Accuracy and Precision were 69.63% and 64.52%, respectively, when using only the TDX/TSX SAR intensity, while they increase to values 78.65% for the Overall Accuracy and 82.08% for the Precision when the Bist. TDX/TSX InSAR Coh. maps were added together with the intensity images as input data. The exploitation of Bist. TDX/TSX InSAR Coh. has been particularly beneficial to reduce the under-detection in vegetated areas and at the same time to reduce the over-detection in urban areas.

In this study, we demonstrated the capacity of bistatic (X-band) short wavelength InSAR coherence to improve flood mapping in a complex environment that contains vegetation and urban areas. This finding can be of extreme interest in the fields of hydrology because in vegetated areas the presence of flood water is usually under-detected using SAR-based algorithms, especially when shorter wavelength sensors are available. In particular, higher accuracy flood extent maps in urban and vegetated areas are of high value for flood prediction models as these flood maps can be used to better calibrate and evaluate models and further improve model forecasts via data assimilation.

Author Contributions: C.C. wrote the manuscript with support from R.A., M.C. and R.H. All of them contributed to the analysis of the results and they provided valuable remarks and constructive feedback. C.C. performed the classification with the help of M.C. and R.A. R.H. assisted in the LISFLOOD-FP model generation. K.C. afforded the high-resolution LiDAR DEM, the bathymetric data and the manually extracted flood extent from very high-resolution GeoEye-1 optical image. He also shared his knowledge about the study region.

Funding: R.H. and M.C. work was funded by the National Research Fund of Luxembourg (FNR) through the MOSQUITO project, grant number C15/SR/10380137.

Acknowledgments: The authors wish to thank the Quebec Environment Department for providing the needed data for the hydraulic model generation. The authors would also like to acknowledge TanDEM-X Science Service System for accepting the proposal (ID HYDR7130) and providing the TanDEM-X/TerraSAR-X bistatic high-resolution SAR images.

Conflicts of Interest: The authors declare that there are no conflicts of interest regarding the publication of this paper.

References

1. *The Human Cost of Weather-Related Disasters 1995-2015*; Technical Report; Centre for Research on the Epidemiology of Disasters (CRED); UN Office for Disaster Risk Reduction (UNISDR): Geneva, Switzerland, 2015.
2. *Estimate of the Average Annual Cost for Disaster Financial Assistance Arrangements due to Weather Events*; Technical Report; Parliamentary Budget Officer: Ottawa, ON, Canada, 2016.
3. *Rapport D'évènement—Inondations Printanières Montérégie 2011*; Technical Report; Organisation de la Sécurité Civile du Québec, Bibliothèque et Archives Nationales du Québec: Québec, QC, Canada, 2013.
4. Rahman, M.S.; Di, L. The state of the art of spaceborne remote sensing in flood management. *Nat. Hazards* **2017**, *85*, 1223–1248. [[CrossRef](#)]
5. Matgen, P.; Hostache, R.; Schumann, G.; Pfister, L.; Hoffmann, L.; Savenije, H. Towards an automated SAR-based flood monitoring system: Lessons learned from two case studies. *Phys. Chem. Earth Part B* **2011**, *36*, 241–252. [[CrossRef](#)]
6. Landuyt, L.; Wesemael, A.; Schumann, G.J.P.; Hostache, R.; Verhoest, N.E.C.; Van Coillie, F.M.B. Synthetic Aperture Radar based flood mapping: an assessment of established approaches. *IEEE Trans. Geosci. Remote Sens.* **2018**, in press. [[CrossRef](#)]

7. Martinis, S.; Kersten, J.; Twele, A. A fully automated TerraSAR-X based flood service. *ISPRS J. Photogramm. Remote Sens.* **2015**, *104*, 203–212. [[CrossRef](#)]
8. Pulvirenti, L.; Chini, M.; Pierdicca, N.; Guerriero, L.; Ferrazzoli, P. Flood monitoring using multi-temporal COSMO-SkyMed data: Image segmentation and signature interpretation. *Remote Sens. Environ.* **2011**, *115*, 990–1002. [[CrossRef](#)]
9. Giustarini, L.; Hostache, R.; Matgen, P.; Schumann, G.J.P.; Bates, P.D.; Mason, D.C. A Change Detection Approach to Flood Mapping in Urban Areas Using TerraSAR-X. *IEEE Trans. Geosci. Remote Sens.* **2013**, *51*, 2417–2430. [[CrossRef](#)]
10. Hostache, R.; Matgen, P.; Wagner, W. Change detection approaches for flood extent mapping: How to select the most adequate reference image from online archives? *Int. J. Appl. Earth Obs. Geoinf.* **2012**, *19*, 205–213. [[CrossRef](#)]
11. Chini, M.; Hostache, R.; Giustarini, L.; Matgen, P. A Hierarchical Split-Based Approach (HSBA) for parametric thresholding of SAR images: flood inundation as a test case. *IEEE Trans. Geosci. Remote Sens.* **2017**, *55*, 6975–6988. [[CrossRef](#)]
12. Lu, J.; Giustarini, L.; Xiong, B.; Zhao, L.; Jiang, Y.; Kuang, G. Automated flood detection with improved robustness and efficiency using multi-temporal SAR data. *Remote Sens. Lett.* **2014**, *5*, 240–248. [[CrossRef](#)]
13. Giustarini, L.; Vernieuwe, H.; Verwaeren, J.; Chini, M.; Hostache, R.; Matgen, P.; Verhoest, N.; de Baets, B. Accounting for Image Uncertainty in SAR-based Flood Mapping. *Int. J. Appl. Earth Obs. Geoinf.* **2015**, *34*, 70–77. [[CrossRef](#)]
14. Giustarini, L.; Hostache, R.; Kavetski, D.; Chini, M.; Corato, G.; Schlaffer, S.; Matgen, P. Probabilistic Flood Mapping Using Synthetic Aperture Radar Data. *IEEE Trans. Geosci. Remote Sens.* **2016**, *54*, 6958–6969. [[CrossRef](#)]
15. Schlaffer, S.; Chini, M.; Giustarini, L.; Matgen, P. Probabilistic mapping of flood-induced backscatter changes in SAR time series. *Int. J. Appl. Earth Obs. Geoinf.* **2017**, *56*, 77–87. [[CrossRef](#)]
16. Bazi, Y.; Bruzzone, L.; Melgani, F. An unsupervised approach based on the generalized Gaussian model to automatic change detection in multitemporal SAR images. *IEEE Trans. Geosci. Remote Sens.* **2005**, *43*, 874–887. [[CrossRef](#)]
17. Kittler, J.; Illingworth, J. Minimum error thresholding. *Pattern Recognit.* **1986**, *19*, 41–47. [[CrossRef](#)]
18. Pulvirenti, L.; Pierdicca, N.; Chini, M.; Guerriero, L. Monitoring flood evolution in vegetated areas using COSMO-SkyMed data: The Tuscany 2009 case study. *IEEE J. Sel. Top. Appl. Earth Obs. Remote Sens.* **2013**, *6*, 1807–1816. [[CrossRef](#)]
19. Pierdicca, N.; Pulvirenti, L.; Chini, M. Flood Mapping in Vegetated and Urban Areas and Other Challenges: Models and Methods. In *Flood Monitoring through Remote Sensing*; Refice, A., D'Addabbo, A., Capolongo, D., Eds.; Springer: Cham, Switzerland, 2018; pp. 135–179.
20. Pierdicca, N.; Pulvirenti, L.; Chini, M.; Guerriero, L.; Candela, L. Observing floods from space: Experience gained from COSMO-SkyMed observations. *Acta Astronaut.* **2013**, *84*, 122–133. [[CrossRef](#)]
21. Mason, D.C.; Giustarini, L.; Garcia-Pintado, J.; Cloke, H.L. Detection of flooded urban areas in high resolution Synthetic Aperture Radar images using double scattering. *Int. J. Appl. Earth Obs. Geoinf.* **2014**, *28*, 150–159. [[CrossRef](#)]
22. Chini, M.; Pulvirenti, L.; Pierdicca, N. Analysis and interpretation of the COSMO-SkyMed observations of the 2011 Japan tsunami. *IEEE Geosci. Remote Sens. Lett.* **2012**, *9*, 467–471. [[CrossRef](#)]
23. Pulvirenti, L.; Chini, M.; Pierdicca, N.; Boni, G. Use of SAR data for detecting floodwater in urban and agricultural areas: The role of the interferometric coherence. *IEEE Trans. Geosci. Remote Sens.* **2016**, *54*, 1532–1544. [[CrossRef](#)]
24. Selmi, S.; Abdallah, W.B.; Abdelfatteh, R. Flood mapping using InSAR coherence map. *Int. Arch. Photogramm. Remote Sens. Spat. Inform. Sci.* **2014**, *40*, 161. [[CrossRef](#)]
25. Chaabani, C.; Abdelfattah, R. Optimized fuzzy algorithm based on modified similarity measure for mapping flood impacts. In Proceedings of the 2016 IEEE International Geoscience and Remote Sensing Symposium (IGARSS), Beijing, China, 10–15 July 2016; pp. 2380–2383.
26. Chaabani, C.; Abdelfattah, R. InSAR Coherence-Dependent Fuzzy C-Means Flood Mapping Using Particle Swarm Optimization. In *International Conference on Advanced Concepts for Intelligent Vision Systems*; Springer: Cham, Switzerland, 2017; pp. 337–348.

27. Martone, M.; Rizzoli, P.; Krieger, G. Volume decorrelation effects in TanDEM-X interferometric SAR data. *IEEE Geosci. Remote Sens. Lett.* **2016**, *13*, 1812–1816. [[CrossRef](#)]
28. Rizzoli, P.; Martone, M.; Gonzalez, C.; Wecklich, C.; Tridon, D.B.; Bräutigam, B.; Bachmann, M.; Schulze, D.; Fritz, T.; Huber, M.; et al. Generation and performance assessment of the global TanDEM-X digital elevation model. *ISPRS J. Photogramm. Remote Sens.* **2017**, *132*, 119–139. [[CrossRef](#)]
29. Martone, M.; Rizzoli, P.; Wecklich, C.; González, C.; Bueso-Bello, J.L.; Valdo, P.; Schulze, D.; Zink, M.; Krieger, G.; Moreira, A. The global forest/non-forest map from TanDEM-X interferometric SAR data. *Remote Sens. Environ.* **2018**, *205*, 352–373. [[CrossRef](#)]
30. Plan Stratégique de Développement Durable Vision D’avenir 360 Portrait du Territoire. Technical Report. Administration Municipale de Saint-Jean-sur-Richelieu, Ville de Saint-Jean-sur-Richelieu 2015. Available online: <http://ville.saint-jean-sur-richelieu.qc.ca/planification-strategique/Documents/diagnostic-portrait-20151009.pdf> (accessed on 9 October 2015).
31. Riboust, P.; Brissette, F. Analysis of Lake Champlain/Richelieu River’s historical 2011 flood. *Can. Water Resour. J.* **2016**, *41*, 174–185. [[CrossRef](#)]
32. Tanguy, M.; Chokmani, K.; Bernier, M.; Poulin, J.; Raymond, S. River flood mapping in urban areas combining Radarsat-2 data and flood return period data. *Remote Sens. Environ.* **2017**, *198*, 442–459. [[CrossRef](#)]
33. Krieger, G.; Moreira, A.; Fiedler, H.; Hajnsek, I.; Werner, M.; Younis, M.; Zink, M. TanDEM-X: A satellite formation for high-resolution SAR interferometry. *IEEE Trans. Geosci. Remote Sens.* **2007**, *45*, 3317–3341. [[CrossRef](#)]
34. Hostache, R.; Matgen, P.; Giustarini, L.; Teferle, F.N.; Tailliez, C.; Iffly, J.F.; Corato, G. A drifting GPS buoy for retrieving effective riverbed bathymetry. *J. Hydrol.* **2015**, *520*, 397–406. [[CrossRef](#)]
35. Martone, M.; Bräutigam, B.; Rizzoli, P.; Gonzalez, C.; Bachmann, M.; Krieger, G. Coherence evaluation of TanDEM-X interferometric data. *ISPRS J. Photogramm. Remote Sens.* **2012**, *73*, 21–29. [[CrossRef](#)]
36. Breiman, L. Random forests. *Mach. Learn.* **2001**, *45*, 5–32. [[CrossRef](#)]
37. Myint, S.W.; Okin, G.S. Modelling land-cover types using Multiple Endmember Spectral Mixture Analysis in a desert city. *Int. J. Remote Sens.* **2009**, *30*, 2237–2257. [[CrossRef](#)]
38. Liu, T.; Yang, X. Mapping vegetation in an urban area with stratified classification and multiple endmember spectral mixture analysis. *Remote Sens. Environ.* **2013**, *133*, 251–264. [[CrossRef](#)]
39. Sonobe, R.; Tani, H.; Wang, X.; Kobayashi, N.; Shimamura, H. Random forest classification of crop type using multi-temporal TerraSAR-X dual-polarimetric data. *Remote Sens. Lett.* **2014**, *5*, 157–164. [[CrossRef](#)]
40. Dubeau, P.; King, D.J.; Unbushe, D.G.; Rebelo, L.M. Mapping the Dabus Wetlands, Ethiopia, Using Random Forest Classification of Landsat, PALSAR and Topographic Data. *Remote Sens.* **2017**, *9*, 1056. [[CrossRef](#)]
41. Feng, Q.; Gong, J.; Liu, J.; Li, Y. Flood mapping based on multiple endmember spectral mixture analysis and random forest classifier—The case of Yuyao, China. *Remote Sens.* **2015**, *7*, 12539–12562. [[CrossRef](#)]
42. Wohlfart, C.; Winkler, K.; Wendleder, A.; Roth, A. TerraSAR-X and Wetlands: A Review. *Remote Sens.* **2018**, *10*, 916. [[CrossRef](#)]
43. Waske, B.; van der Linden, S. Classifying multilevel imagery from SAR and optical sensors by decision fusion. *IEEE Trans. Geosci. Remote Sens.* **2008**, *46*, 1457–1466. [[CrossRef](#)]
44. Pierdicca, N.; Chini, M.; Pelliccia, F. The contribution of SIASGE radar data integrated with optical images to support thematic mapping at regional scale. *IEEE J. Sel. Top. Appl. Earth Obs. Remote Sens.* **2014**, *7*, 2821–2833. [[CrossRef](#)]
45. Aggarwal, C.C. Data Mining: The Textbook. Springer Publishing Company, Incorporated, 2015. Available online: <https://www.springer.com/de/book/9783319141411> (accessed on 1 January 2015).
46. Breiman, L. Bagging predictors. *Mach. Learn.* **1996**, *24*, 123–140. [[CrossRef](#)]
47. Safavian, S.R.; Landgrebe, D. A survey of decision tree classifier methodology. *IEEE Trans. Syst. Man Cybern.* **1991**, *21*, 660–674. [[CrossRef](#)]
48. Bates, P.D.; De Roo, A. A simple raster-based model for flood inundation simulation. *J. Hydrol.* **2000**, *236*, 54–77. [[CrossRef](#)]
49. Horritt, M.; Bates, P. Evaluation of 1D and 2D numerical models for predicting river flood inundation. *J. Hydrol.* **2002**, *268*, 87–99. [[CrossRef](#)]
50. Afshari, S.; Tavakoly, A.A.; Rajib, M.A.; Zheng, X.; Follum, M.L.; Omranian, E.; Fekete, B.M. Comparison of new generation low-complexity flood inundation mapping tools with a hydrodynamic model. *J. Hydrol.* **2018**, *556*, 539–556. [[CrossRef](#)]

51. Neal, J.; Schumann, G.; Fewtrell, T.; Budimir, M.; Bates, P.; Mason, D. Evaluating a new LISFLOOD-FP formulation with data from the summer 2007 floods in Tewkesbury, UK. *J. Flood Risk Manag.* **2011**, *4*, 88–95. [[CrossRef](#)]
52. Van der Sande, C.; De Jong, S.; De Roo, A. A segmentation and classification approach of IKONOS-2 imagery for land cover mapping to assist flood risk and flood damage assessment. *Int. J. Appl. Earth Obs. Geoinf.* **2003**, *4*, 217–229. [[CrossRef](#)]
53. Wood, M.; Hostache, R.; Neal, J.; Wagener, T.; Giustarini, L.; Chini, M.; Corato, G.; Matgen, P.; Bates, P. Calibration of channel depth and friction parameters in the LISFLOOD-FP hydraulic model using medium-resolution SAR data and identifiability techniques. *Hydrol. Earth Syst. Sci.* **2016**, *20*, 4983. [[CrossRef](#)]
54. Hostache, R.; Chini, M.; Giustarini, L.; Neal, J.; Kavetski, D.; Wood, M.; Corato, G.; Pelich, R.M.; Matgen, P. Near-Real-Time Assimilation of SAR-Derived Flood Maps for Improving Flood Forecasts. *Water Resour. Res.* **2018**, *54*, 5516–5535. [[CrossRef](#)]
55. Hostache, R.; Hissler, C.; Matgen, P.; Guignard, G.; Bates, P. Modelling suspended-sediment propagation and related heavy metal contamination in floodplains: a parameter sensitivity analysis. *Water Resour. Res.* **2014**, *18*, 3539–3551.
56. Oubennaceur, K.; Chokmani, K.; Nastev, M.; Tanguy, M.; Raymond, S. Uncertainty Analysis of a Two-Dimensional Hydraulic Model. *Water* **2018**, *10*, 272. [[CrossRef](#)]
57. Congalton, R.G. A review of assessing the accuracy of classifications of remotely sensed data. *Remote Sens. Environ.* **1991**, *37*, 35–46. [[CrossRef](#)]
58. Brisco, B.; Schmitt, A.; Murnaghan, K.; Kaya, S.; Roth, A. SAR polarimetric change detection for flooded vegetation. *Int. J. Digit. Earth* **2013**, *6*, 103–114. [[CrossRef](#)]
59. Chini, M.; Papastergios, A.; Pulvirenti, L.; Pierdicca, N.; Matgen, P.; Parcharidis, I. SAR coherence and polarimetric information for improving flood mapping. In Proceedings of the 2016 IEEE International Geoscience and Remote Sensing Symposium (IGARSS), Beijing, China, 10–15 July 2016; pp. 7577–7580.



© 2018 by the authors. Licensee MDPI, Basel, Switzerland. This article is an open access article distributed under the terms and conditions of the Creative Commons Attribution (CC BY) license (<http://creativecommons.org/licenses/by/4.0/>).